

Mapping Water Exchange Rates in Rat Tumor Xenografts Using the Late-Stage Uptake Following Bolus Injections of Contrast Agent

Colleen Bailey,^{1,2*} Firas Moosvi,^{1,2} and Greg J. Stanisz^{1,2}

Purpose: To map the intra-to-extracellular water exchange rate constant in rat xenografts using a two-compartment model of relaxation with water exchange and a range of contrast agent concentrations and compare with histology.

Methods: MDA-MB-231 cells were xenografted into six nude rats. Three bolus injections of gadodiamide were administered. When uptake in the tumor demonstrated a steady-state, T_1 data were acquired by spoiled gradient recalled acquisitions at four flip angles. A global fit of data to a two-compartment model incorporating exchange was performed, assuming a distribution volume of 20% of the rat.

Results: Voxels that did not reach steady-state and were excluded from parametric maps tended to be in large necrotic areas. TUNEL-negative (nonapoptotic) regions tended to have well-defined error bounds, with an average intra-to-extracellular exchange rate constant of 0.6 s^{-1} . Apoptotic regions had higher exchange, but poorly determined upper bounds, with goodness of fit similar to that for a model assuming infinitely fast exchange. A lower bound of $>3 \text{ s}^{-1}$ was used to establish voxels where the exchange rate constant was fast despite a large upper bound.

Conclusion: Water exchange rates were higher in apoptotic regions, but examination of statistical errors was an important step in the mapping process. **Magn Reson Med** 71:1874–1887, 2014. © 2013 Wiley Periodicals, Inc.

Key words: water exchange rate; DCE-MRI; tumor response; quantitative MRI; two-compartment model

Response of cancer patients to treatment is highly variable and imaging markers offer potential to distinguish patients responding well to therapy from those responding poorly (1). In particular, rates of apoptotic cell death correlate well with tumor reduction (2,3).

In vitro, the rate of water exchange across the cell membrane increases in apoptotic cells mainly as a result of increased membrane permeability to water, although changes in cell shape and size due to membrane bleb-

bing may also contribute (4). However, the method used to measure the water exchange rate constant in vitro relies on the addition of known concentrations of contrast agent to the extracellular space and measurements of multiple points along the T_1 relaxation curve, procedures which are challenging in vivo. In addition, the precision with which the water exchange rate constant can be estimated depends on the concentration of gadolinium (Gd) contrast agent present, with low concentrations producing fits that have low sensitivity to exchange (5–7). The Gd concentration in a tissue region varies with the blood supply and relative fraction of extracellular water (related to cellularity), further complicating in vivo attempts to detect the effects of water exchange reliably.

To measure the transmembrane exchange rate in vivo, this study makes use of the period following contrast agent injection when the tissue uptake curve remains nearly constant, a steady-state concentration region. During this time, the T_1 relaxation is characterized with a spoiled gradient recalled (SPGR) sequence with four flip angles (8), a relatively fast T_1 characterization method that can be completed in ~ 1 min. The measurements are repeated following three separate injections and the contrast agent concentration is approximated based on the injection amount. This yields T_1 relaxation data at four separate Gd concentrations (precontrast and following each of the three injections), which can be fitted to a two-compartment model of relaxation with exchange (9). Fitting each voxel in the image with this model, a map of the intra-to-extracellular water exchange rate constant, k_{IE} , is generated and this is compared to histology. The conditions under which this method is valid and the errors in the fit parameters are examined.

THEORY

Two-Compartment Model of Relaxation with Exchange

A simple model of cells considers the water in two separate compartments, the intracellular (I) and extracellular (E) spaces, as shown in Figure 1. Each compartment contains a different fraction of the total water, M_{0I} and M_{0E} , which are related by $M_{0I} + M_{0E} = 1$. The environment in each compartment is also different, resulting in different relaxation rate constants, $R_{1I} = 1/T_{1I}$ and $R_{1E} = 1/T_{1E}$. However, water is not confined to a particular compartment during relaxation; it moves across the cell membrane at a rate dictated by the exchange constant k_{IE} for movement from intracellular to extracellular space, and at a rate k_{EI} for movement from extracellular to intracellular space. These rates are related by the equilibrium condition $M_{0I}k_{IE} = M_{0E}k_{EI}$.

¹Department of Medical Biophysics, Faculty of Medicine, University of Toronto, Toronto, Canada.

²Department of Imaging Research, Sunnybrook Health Sciences Centre, Toronto, Canada.

Additional Supporting Information may be found in the online version of this article.

Grant sponsor: Natural Sciences and Engineering Research Council of Canada.

*Correspondence to: Colleen Bailey, Ph.D., Sunnybrook Health Sciences Centre, 2075 Bayview Ave., S-Wing, 6th Floor, Rm S605, Toronto, ON, Canada M4N 3M5. E-mail: colleen.bailey@sri.utoronto.ca

Received 21 December 2012; revised 3 May 2013; accepted 26 May 2013
DOI 10.1002/mrm.24847

Published online 25 June 2013 in Wiley Online Library (wileyonlinelibrary.com).

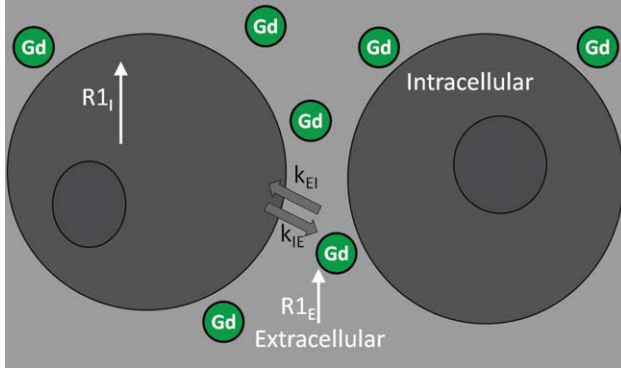


FIG. 1. Two-compartment model of water relaxation with exchange across the cell membrane (signal from the plasma is assumed to be negligible). The intracellular space, I , and extracellular space, E , have different water fractions, M_{0I} and $M_{0E} = 1 - M_{0I}$, depicted by the sizes of the dark and light gray regions. Each compartment has a longitudinal relaxation rate constant, R_{1I} and R_{1E} , where R_{1E} varies based on the concentration of contrast agent in the extracellular space. Water exchanges from the intra- to extracellular space at a rate described by the constant k_{IE} and from the extracellular to the intracellular space at the related rate k_{EI} .

The change in magnetization in each compartment may therefore either be due to T_1 relaxation of water or to water movement across the cell membrane. It is assumed that the sequence used to characterize T_1 relaxation has a short enough echo time that transverse relaxation (T_2) effects are negligible. The Bloch equations for the longitudinal z -magnetization in the intracellular and extracellular compartments are then (9):

$$\frac{dM_{ZI}}{dt} = R_{1I}(M_{0I} - M_{ZI}) - k_{IE}M_{ZI} + k_{EI}M_{ZE} \quad [1]$$

$$\frac{dM_{ZE}}{dt} = R_{1E}(M_{0E} - M_{ZE}) - k_{EI}M_{ZE} + k_{IE}M_{ZI} \quad [2]$$

These coupled differential equations can be solved analytically to give two relaxation rate constants, R_{1A} and R_{1B} , and two coefficients, M_{0A} and M_{0B} . These parameters do not generally describe physically distinct compartments (though they may at the extreme limits of exchange), but rather are combinations of the parameters in the two-compartment model described above:

$$R_{1A} = \frac{R_{1I} + R_{1E} + k_{IE} + k_{EI} + \sqrt{(R_{1I} - R_{1E} + k_{IE} - k_{EI})^2 + 4(k_{IE}k_{EI})}}{2} \quad [3]$$

$$R_{1B} = \frac{R_{1I} + R_{1E} + k_{IE} + k_{EI} - \sqrt{(R_{1I} - R_{1E} + k_{IE} - k_{EI})^2 + 4(k_{IE}k_{EI})}}{2} \quad [4]$$

$$M_{0A} = \frac{1}{2} - \frac{1}{2} \frac{(R_{1I} - R_{1E})(M_{0E} - M_{0I}) + k_{EI} + k_{IE}}{\sqrt{(R_{1I} - R_{1E} + k_{IE} - k_{EI})^2 + 4k_{IE}k_{EI}}} \quad [5]$$

$$M_{0B} = 1 - M_{0A} \quad [6]$$

For the SPGR sequence used in this study, the signal equation has one term for each of the relaxation rate components, weighted by the M_{0A} and M_{0B} coefficients:

$$S = S_0 \left[M_{0A} \frac{1 - e^{-TR \cdot R_{1A}}}{1 - e^{-TR \cdot R_{1A}} \cos(f_{acc} \alpha)} \sin(f_{acc} \alpha) + M_{0B} \frac{1 - e^{-TR \cdot R_{1B}}}{1 - e^{-TR \cdot R_{1B}} \cos(f_{acc} \alpha)} \sin(f_{acc} \alpha) \right] \quad [7]$$

where S_0 is the equilibrium signal when all magnetization is flipped into the transverse plane, TR is the repetition time and f_{acc} corrects for deviations from the prescribed flip angle, α .

As f_{acc} can be determined by B_1 correction methods prior to the SPGR experiment, Eq. [4] contains four independent parameters: S_0 , R_{1A} , R_{1B} , $M_{0A} = 1 - M_{0B}$. However there are five independent parameters of interest in the two-compartment model: S_0 , R_{1I} , R_{1E} , M_{0E} , and k_{IE} . Altering one of the two-compartment parameters in a known way, for example changing relaxation rate using contrast agents (10,11), yields multiple datasets where Eq. [4] applies and these may be solved globally for the remaining two-compartment model parameters.

Contrast Agent as a Method of Probing the Two-Compartment Model Parameters

The contrast agent Gd diethylenetriamine pentaacetic acid bis-methylamide (Gd-DTPA-BMA, gadodiamide) is an extracellular contrast agent that alters the T_1 relaxation rate of water in that compartment:

$$R_{1E} = R_{1E0} + r_1[\text{Gd}]_E \quad [8]$$

where R_{1E0} is the relaxation rate constant in the absence of gadodiamide and r_1 is the relaxivity. This equation assumes that the extracellular space is well-mixed so that all of the water in that compartment experiences the same increase in relaxation rate due to gadodiamide. The addition of gadodiamide therefore perturbs the values of R_{1A} , R_{1B} , M_{0A} and M_{0B} (described by Eqs. [3]–[6]), thus affecting the signal as a function of flip angle (see Eq [7]).

In the limit where

$$k_{IE} \left(1 + \frac{M_{0I}}{M_{0E}} \right) \gg |R_{1I} - R_{1E}| \quad [9]$$

Eqs. [3]–[6] simplify as M_{0A} approaches zero and M_{0B} approaches 1, so that the relaxation is monoexponential with a relaxation rate constant

$$R_{1B} = M_{0I} \cdot R_{1I} + M_{0E} \cdot R_{1E} \equiv R_{1FXL} \quad [10]$$

This is known as the fast exchange limit (FXL) (5) and substituting Eq. [8] in Eq. [10] gives

$$R_{1FXL} = M_{0I} \cdot R_{1I} + M_{0E} \cdot R_{1E0} + M_{0E} r_1 [\text{Gd}]_E \quad [11]$$

The relaxation rate constant, R_1 , changes linearly with the Gd concentration so long as the FXL condition (Eq. [9]) holds. The value of k_{IE} does not appear in these equations because the fit is insensitive to it (the exchange rate is too fast relative to the relaxation process). In most biological tissues in the absence of Gd, $R_{1I} \sim R_{1E}$ and Eq. [9] is valid. It is the addition of Gd that alters the balance between water exchange and

magnetization recovery by T_1 . When sufficient Gd is added such that $k_{TE} \left(1 + \frac{M_{0I}}{M_{0E}}\right) \sim |R_{1I} - R_{1E}|$, the relaxation becomes nonmonoexponential and the measured relaxation rate constants are not linear with Gd concentration. In summary, the Gd concentration affects the reliability of the exchange estimate, which is important in determining where in the tumor the estimates are reliable and some regions may need to be excluded from analysis.

Contrast Agent Concentration at Steady-State

Following a bolus injection, the contrast agent leaks across the vessel wall into the extracellular space, resulting in a concentration that changes significantly over the course of several minutes (see Supporting Information Fig. S1). It then reaches a maximum and begins to wash out. In many tumors, this washout is a slow process, producing a steady-state region of contrast agent concentration.

When the extracellular concentration (or equivalently the relaxation rate) reaches a maximum, the concentrations in the plasma and extracellular spaces are equal: $[Gd]_p = [Gd]_e$, assuming that the contrast agent moves across the vessel wall according to Fick's law and that the plasma and extracellular compartments are well-mixed (12). At steady-state, the contrast agent concentration in the plasma is proportional to the amount injected with a constant of proportionality that depends on the fraction of the rat's volume that is accessible to contrast agent, the distribution volume, V_{dist} . The effect of clearance can be accounted for if the time constant for clearance of the contrast agent, T_{clear} , is known. This provides a means of approximating the contrast agent concentration in the extracellular space based on the amount of gadodiamide injected:

$$[Gd]_E = [Gd]_p = \sum_{k=1}^{N_{inj}} \frac{V_{inj,k} [Gd]_{inj}}{V_{dist}} \exp(-t_{elapsed,k} / T_{clear}) \quad [12]$$

where the amount of gadodiamide from the k th injection is equal to the volume of that injection, $V_{inj,k}$, multiplied by the concentration of gadodiamide, $[Gd]_{inj}$. This is corrected for clearance using the time that has passed between the k th injection and the steady-state measurement, $t_{elapsed,k}$. As this time differs for each injection, the cumulative amount is the sum of these terms for each of the completed injections, numbering N_{inj} .

In this study, it was assumed that the distribution volume was equal to 20% of the rat's volume, calculated from the rat's mass and a density of 1 g/mL. The clearance time, T_{clear} , was assumed to be 29 min, equivalent to a biological half-life of 20 min, a value based on pharmacokinetic experiments (not shown) and consistent with literature experiments of gadodiamide clearance in rats (13–15). The effects of these assumptions will be discussed later. The extracellular longitudinal relaxation rate, R_{1E} , applied to the two-compartment model was calculated by substituting the $[Gd]_E$ value from Eq. [12] into Eq. [8] with $r_1 = 4.2 \text{ mM}^{-1} \text{ s}^{-1}$ and $R_{1E0} = 0.67 \text{ s}^{-1}$ as determined by previous measurements of contrast agent in the blood plasma at 7 T. It was assumed that

the relaxivity was the same in all extracellular environments.

METHODS

Animal Model

Six female nude rats (6–8 weeks) were injected subcutaneously in the hind limb with ~5 million breast cancer cells (MDA-MB-231). Cells were cultured in Roswell Park Memorial Institute medium (Wisent, Montreal, Canada) with 5% fetal bovine serum (Fisher Scientific, Ottawa, Canada) and 5 mL penicillin and streptomycin (Invitrogen Canada Inc) for 8–17 days (passage two to five) prior to injection.

Tumors were allowed to grow to ~1 cm, which took ~6 weeks. In two cases, cells were implanted with matrigel and four rats were treated with 8 Gy radiation to induce cell death. Only results immediately prior to sacrifice are presented in this article. For scanning and procedures, animals were anaesthetized with isoflurane (Abbott Laboratories, Montreal, Canada), and experiments were performed under approval of the Sunnybrook Animal Care Committee. The average rat weight was $172 \pm 12 \text{ g}$.

Contrast Injection Procedure

Catheters (24 G gauge, Hospira, Lake Forest, IL) were inserted into the animal's tail vein and attached to a four-way stopcock. Three separate injections of gadodiamide (Omniscan, GE Healthcare) diluted with saline were performed as follows: $V_{inj1} = 0.3 \text{ mL}$, $[Gd]_{inj1} = 167 \text{ mM}$; $V_{inj2} = 0.3 \text{ mL}$, $[Gd]_{inj2} = 333 \text{ mM}$; $V_{inj3} = 0.3 \text{ mL}$, $[Gd]_{inj3} = 500 \text{ mM}$. This is a cumulative dose of 1.7 mmol/kg for a 172 g rat. Signal intensity following each injection was monitored by a DCE-MRI sequence of repeated SPGR images and, when signal approached a constant level, steady-state T_1 data were acquired using SPGR scans at four different flip angles. In general, the time between injections was $t_{inj} \sim 6 \text{ min}$, including ~1 min to acquire data at steady-state. Prior to contrast agent administration, four SPGR scans and seven inversion recovery scans using different inversion times were performed for B_1 correction. There are therefore T_1 data at four different gadodiamide concentrations.

MRI Scan Parameters

All MRI scans were performed on a 7 T Bruker Avance (Bruker Biospin, Germany) animal scanner with an 86 mm quadrature coil for excitation and 2 cm surface coil placed around the tumor for receive. To obtain T_1 data, a 3D SPGR sequence was chosen because it is fast (four flip angles can be obtained in ~1 min) and accurate T_1 measurements can be obtained with appropriate flip angles, data fitting procedures and B_1 correction schemes (16,17). At each steady-state concentration, four SPGR scans were acquired ($\alpha = 16.6\text{--}20, 11, 7, \text{ and } 5^\circ$; TR = 20 ms; TE = 2.5 ms; $128 \times 96 \times 8$ matrices; $4 \times 3 \times 0.8 \text{ cm}^3$ field-of-view).

A series of seven 2D inversion recovery scans (inversion time = 62.1, 100, 300, 700, 900, 1200, 1500 ms) was

acquired prior to injection for B_1 correction (TR = 2500 ms; TE = 11.6 ms; 64×96 matrices, 4×3 cm² field of view, 1 mm slice thickness, three slices).

The DCE-MRI sequence used to monitor the contrast agent concentration and its approach to steady state was an SPGR sequence at a single flip angle ($\alpha = 16.6\text{--}20^\circ$; TR = 20 ms; TE = 2.5 ms; $64 \times 96 \times 8$ matrices; $4 \times 3 \times 0.8$ cm³ field-of-view; temporal resolution 10.2 s).

All images were acquired axially with one signal average (NEX). A saturation band (26-mm thick) was placed sagittally with respect to the rat, covering the nonimplanted leg and half of the body, to reduce motion artefacts and limit signal from inflowing blood. No visible respiratory motion was apparent in the images and the phase encode direction was selected to minimize the effects in the tumor region (phase encoding right-to-left direction).

Data Fitting

Motion during the steady-state image acquisition was negligible. However the injections resulted in small displacements that were corrected by manual rigid registration. This method agreed well with a more sophisticated, automated technique that allowed nonrigid rotations and translations (18), with the edges of the tumor shifting less than 0.4 voxels (0.13 mm) after registration for both techniques, compared to a 0.9 voxel (0.28 mm) shift for unregistered data.

Errors in the prescribed flip angle were calculated using the precontrast inversion recovery data. The data from all seven inversion times were fitted to an equation for mono-exponential T_1 relaxation assuming Gaussian noise (19):

$$S_{\text{IR}} = S_{\text{eq}}[1 - (1 + a)e^{-TR/R_{10}} + ae^{-TR/R_{10}}] \quad [13]$$

where S_{eq} is the equilibrium signal, a accounts for imperfections in the 180° pulse and R_{10} is the average longitudinal relaxation rate constant in the absence of gadodiamide. This equation assumes exchange is fast (mono-exponential) when no contrast agent is present and that the echo time, TE, is short enough to neglect T_2 relaxation.

This R_{10} value was then used when fitting the precontrast steady-state SPGR data to

$$S_{\text{SPGR}} = S_0 \left(\frac{1 - e^{-TR/R_{10}}}{1 - e^{-TR/R_{10}} \cos f_{\text{acc}} \alpha} \sin f_{\text{acc}} \alpha \right) \quad [14]$$

to determine the value of f_{acc} , which was fixed in Eq. [7]. This equation assumes that the flip angle error is linear with the prescribed flip angle.

Data from all four flip angles at all four gadodiamide concentrations ($[\text{Gd}] = 0$ mM and during the steady-state following each of the three injections) were fitted globally to Eq. [7], with R_{1A} , R_{1B} , M_{0A} and M_{0B} given by Eqs. [3]–[6]. This yielded four independent fitted parameters: the equilibrium signal S_0 , the longitudinal relaxation rate constant in the intracellular space R_{1I} , the extracellular water fraction M_{0E} and the water exchange rate constant from the intracellular to the extracellular space k_{IE} . The

longitudinal relaxation rate constant in the extracellular space, R_{1E} , was assumed to vary in a manner dependent on the amount of gadodiamide injected, as described in the theory section (Eqs. [8] and [12]).

For comparison, data were also fitted to the limits of Eq. [7]. In the FXL, Eq. [7] reduces to:

$$S = S_0 \frac{1 - e^{-TR/R_{1\text{FXL}}}}{1 - e^{-TR/R_{1\text{FXL}} \cos f_{\text{acc}} \alpha}} \sin f_{\text{acc}} \alpha \quad [15]$$

where $R_{1\text{FXL}}$ is the weighted average of the extracellular and intracellular R_1 s (Eq. [11]). Then data were fitted assuming that no exchange of intra-to-extracellular water occurred on the timescale of relaxation (slow exchange limit, SXL):

$$S = S_0 \left[M_{0E} \frac{1 - e^{-TR/R_{1E}}}{1 - e^{-TR/R_{1E}} \cos f_{\text{acc}} \alpha} \sin f_{\text{acc}} \alpha + M_{0I} \frac{1 - e^{-TR/R_{1I}}}{1 - e^{-TR/R_{1I}} \cos f_{\text{acc}} \alpha} \sin f_{\text{acc}} \alpha \right] \quad [16]$$

Error Analysis

Statistical errors in the fitted parameters were determined by adjusting the parameter of interest in small increments and allowing the remaining parameters to vary until

$$\chi^2 \geq \chi_0^2 \left[1 + \frac{n_p}{N - n_p} F(n_p, N - n_p, 0.68) \right] \quad [17]$$

where χ^2 is the reduced chi-squared value from the fit with one fixed parameter, χ_0^2 is the reduced chi-squared value with all parameters optimized, n_p is the number of parameters in the fit, N is the number of data points and F is the F distribution function, calculated here for a 68% confidence interval (20).

Mapping and Exclusion Criteria

Parametric maps of the two-pool model parameters were generated by fitting the inversion recovery data voxel-by-voxel according to Eq. [13] and then upsampling using a nearest-neighbor approach to match the resolution of the steady-state data. A flip angle correction factor, f_{acc} , was calculated using Eq. [14] for each voxel and fixed in Eqs. [3]–[7] while the data were fitted for the remaining two-compartment model parameters (S_0 , R_{1I} , M_{0E} and k_{IE}).

It must be noted, however, that the parameters of the two-compartment model may be difficult to determine in some regions of the tumor. Fitting to the model requires that the contrast agent concentration is steady during data acquisition, but the arrival of the bolus and the rate of clearance vary depending on the leakiness of the blood vessels and the available space into which the contrast agent leaks. The final maps therefore excluded points that did not reach steady-state by eliminating voxels in which the change in signal over the last 1.4 min of the first DCE monitoring sequence was more than 15 times the standard deviation of the noise, SD_{noise} .

There are also regions with limited gadodiamide uptake. The value of exchange is poorly determined in these regions (5–7) since the relaxation rate changed

very little and the tissue remained near the FXL. Using a simple signal change threshold to determine when the model is reliable is problematic because the change in signal that is needed for reliable parameter determination depends on several factors, including the amount of contrast agent delivered, the water fractions and the value of exchange itself. Instead, these regions were identified by using Eq. [17] to determine whether the fit was sensitive to the value of the exchange rate parameter. Voxels where the confidence interval for the exchange rate constant was broad (i.e., k_{IE} values from < 3 to $> 5 \text{ s}^{-1}$ did not significantly change the χ^2 value from its minimum) were excluded from the final maps as unreliable. However, in some cases where the confidence interval was broad, it was still possible to place a reasonable lower bound on the exchange rate constant ($k_{IE} > 3 \text{ s}^{-1}$). Values where the lower bound of the confidence interval was $> 3 \text{ s}^{-1}$ were therefore included in the parametric maps even if the upper bound was high since the exchange rate may be said to be high, regardless of the fact that the exact value is poorly determined.

DCE Data Fitting

The DCE monitoring data were fitted to a standard Kety–Tofts model (12,21) relating the concentration of contrast agent in the tissue, C_t , to that in the plasma, C_p , to yield the volume transfer constant, K_{trans} , and the extravascular extracellular volume fraction, v_e .

$$C_t(t) = K_{trans} \int_{\tau=0}^t C_p(\tau) e^{-\frac{K_{trans}(t-\tau+t_{lag})}{v_e}} d\tau \quad [18]$$

The parameter t_{lag} accounts for the delay between the bolus arrival in the plasma and the arrival in the tissue, where interpolation between data points was done linearly. It is possible to fit DCE-MRI data to models incorporating water exchange, as in Refs. (5–7) and (22–25), but a simpler model was chosen here due to the limited temporal resolution and lack of arterial input function. A biexponential function was used for the plasma concentrations:

$$C_p = D(A_1 e^{-k_1 t} + A_2 e^{-k_2 t}) \quad [19]$$

where D is the dose of gadodiamide in mmol/kg body weight, $A_1 = 9 \text{ kg/L}$, $A_2 = 5 \text{ kg/L}$, $k_1 = 2 \text{ min}^{-1}$ and $k_2 = 0.05 \text{ min}^{-1}$. These values are taken from separate pharmacokinetic experiments on this strain of rats (data not shown) and agree with the literature values for other rat strains (13–15). Only the data from the first injection were fitted since these involve lower gadodiamide concentrations that are less likely to be biased by errors created by intra-to-extracellular water exchange and because some later uptake curves were compromised by motion.

Histology

All six tumors were examined histologically with one of two methods. Four tumors were placed in a mould, covered in Tissue Tek Optimum Cutting Temperature gel

(Fisher Scientific, Ottawa, Canada) and frozen at -80°C . Levels were cut at 1 mm increments with two slices at each level. The axial orientation of the MRI images was maintained during slicing. One slice was stained with haematoxylin and eosin (H&E) and the other was co-stained with terminal deoxynucleotidyl transferase dUTP nick end labeling (TUNEL) and CD-31, a marker of blood vessel endothelial cells. The remaining two tumors were fixed in formalin and levels cut at 1 mm increments (two slices per level: one H&E, one TUNEL).

Slides were imaged using a Mirax scanner (Carl Zeiss MicroImaging, Göttingen, Germany). MRI was aligned with histology manually by first finding the slice with the largest diameter in both modalities and then assuming preceding and subsequent slices from histology corresponded to those from MRI because of the similar spacing. Although there may be some error due to shrinkage during fixation, the data were typically located near the slice with the largest diameter, which should minimize error and be sufficient for qualitative comparison.

RESULTS

The fits to the two-compartment model were stable and the statistical errors in the fitted parameters were smaller than the standard deviation across the voxels included in the parametric maps for equilibrium signal S_0 , intracellular longitudinal relaxation rate R_{1I} and extracellular water fraction M_{0E} . The fit errors for the water exchange rate constant were often poorly determined, particularly the upper bounds, which is why they have been considered as a special case in the construction of the parametric maps below. The reproducibility in a single rat was demonstrated in the gastrocnemius muscle region of a control animal that was not treated with radiation and was scanned twice 2 days apart. The extracellular water fraction was 0.13 ± 0.06 at baseline and 0.17 ± 0.05 at 48 h. The water exchange rate constant from the intracellular to extracellular space, k_{IE} , was $1.0 \pm 0.5 \text{ s}^{-1}$ at baseline and $1.1 \pm 0.4 \text{ s}^{-1}$ at 48 h.

Signal change due to contrast agent uptake varied between tumors: the average signal on the DCE monitoring images increased $61 \pm 60\%$ from before to after the first injection. It also varied within a single rat's tumor, as demonstrated by Figure 2. The curve at point (b) shows visible signal change due to contrast agent uptake, as well as a steady-state region occurring ~ 1 min after injection and persisting for several minutes. The breaks in the data at ~ 300 and ~ 660 s are the times where steady-state multi-flip angle data were acquired, a process that took ~ 1 min and during which little signal dropoff was visible.

In contrast, the data from voxel (c) do not demonstrate a steady-state within 5 min of injection. Such voxels were eliminated using the second exclusion criterion: over the last 1.4 min of the first DCE-MRI sequence, the change in signal $\Delta S > 15 * SD_{noise}$. The uptake curve of voxel (d) shows a region with very little contrast agent uptake and is excluded based on wide error bounds for the water exchange rate constant.

Because of the exclusion criteria, on average $20 \pm 10\%$ of the voxels within the tumor were included in the

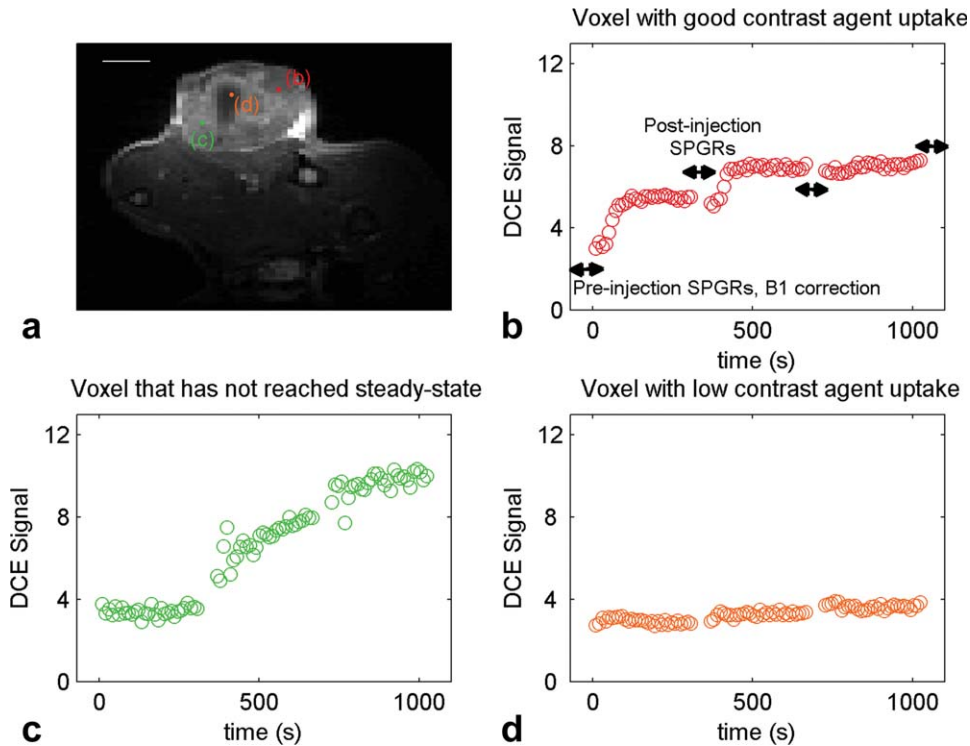


FIG. 2. Contrast agent uptake in rat tumour. The three points in image (a) show different uptake characteristics. Point (b) near the tumour rim has visible change in signal due to contrast agent uptake and reaches steady-state within ~1 min of each injection, remaining there for at least 3 min afterward. Point (c) does not reach steady-state and the two-compartment model cannot be applied in this region. Point (d) shows low contrast agent uptake and the two-compartment model gives a wide range of exchange rate constants that fit the data in these regions. The breaks in the data (horizontal arrows) indicate the time the four SPGRs are acquired at each steady-state concentration. Inversion recovery data are also acquired prior to injection for B_1 correction. Scale bar is 5 mm.

maps. Figure 3 maps the points that have been excluded due to not reaching steady-state (green), excluded due to poorly determined exchange rate constants from low contrast agent uptake (orange) and included in the final parametric maps (red) in one of the animals.

Voxels that were included fall into two cases, as demonstrated by Figures 4 and 5. Figure 4 shows the voxel from (b) in Figure 2, a case where the error bounds on the exchange rate constant are well-defined: $k_{IE} = 0.5 (-0.2/+0.4) s^{-1}$. The steady-state SPGR data for the four flip angles at each of the four gadodiamide concentrations (preinjection and three-post injection) are fitted to the two-compartment, fast exchange and slow exchange models (solid lines), with residuals indicated underneath. The two-compartment model in (a) has small residuals and very little bias in the fit. The fast exchange model in (b) is biased at particular concentrations; for example the fit overestimates the SPGR curve for the lowest concentration, particularly at high flip angles. For this voxel, the slow exchange model fits better than the fast exchange, but more poorly than the two-compartment model ($\chi_{0,FXL}^2 \sim 8 * \chi_{0,2-comp}^2$; $\chi_{0,SXL}^2 \sim 2 * \chi_{0,2-comp}^2$). The extracellular water fractions, M_{0E} , from the fits with the different exchange assumptions follow the pattern $M_{0E,FXL} < M_{0E,2-comp} < M_{0E,SXL}$.

Figure 5 shows data from a different voxel, where the two-compartment and fast exchange models demonstrate similar goodness of fit ($\chi_{0,FXL}^2 \sim \chi_{0,2-comp}^2$). The slow

exchange model was a poor fit ($\chi_{0,SXL}^2 \sim 12 * \chi_{0,2-comp}^2$). The extracellular water fractions from the two-compartment and fast exchange models were similar and lower than that obtained from the slow exchange fit:

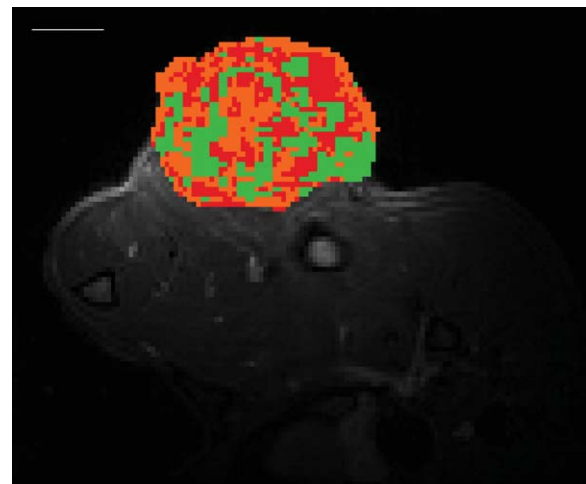


FIG. 3. A map demonstrating the voxels excluded from the final parametric maps because they have not reached steady-state (green) or because there was insufficient contrast agent to determine exchange reliably (orange). Voxels included in the final map (red) tend to cluster near the tumour rim. Scale bar represents 5 mm.

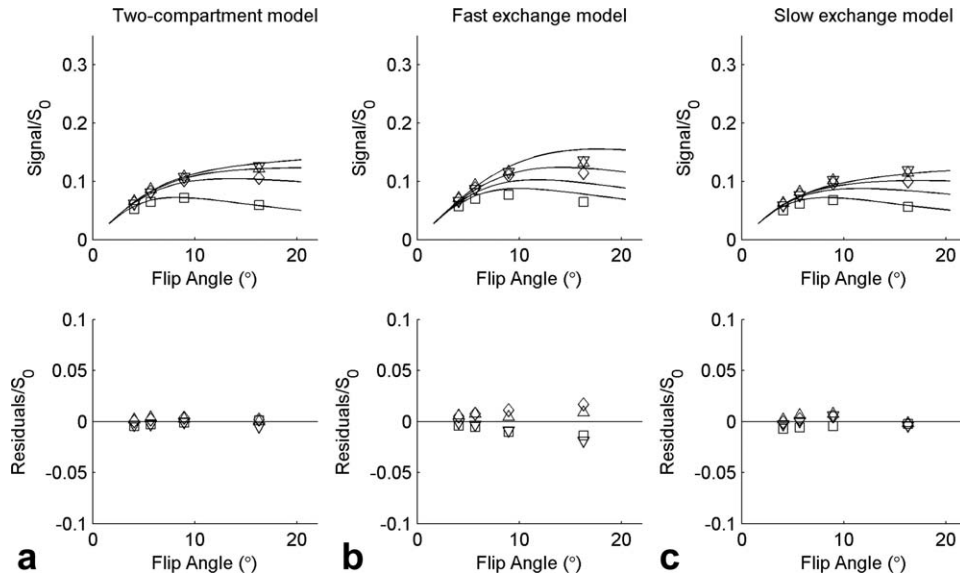


FIG. 4. Steady-state data for voxel (b) from Figure 2 at each of four flip angles and four gadodiamide concentrations (cumulative amounts gadodiamide injected: squares—0 mmol; diamonds—0.05 mmol; triangles—0.15 mmol; inverted triangles—0.3 mmol) with fits (a) to the two-compartment model with water exchange (Eqs. [3]–[7]), (b) assuming infinitely fast exchange of water across the cell membrane (Eq. [15]) and (c) assuming no exchange of water across the cell membrane (Eq. [16]) shown by the solid lines. Residuals are shown underneath the fits to demonstrate both the improved fit (χ_0^2 780% higher for FXL than two-compartment; χ_0^2 160% higher for SXL than two-compartment) and the lower systematic error of the two-compartment model fit. The intra-to-extracellular water exchange rate constant for the two-compartment fit was $k_{IE} = 0.5 (-0.2/+0.4) \text{ s}^{-1}$.

$M_{0E,FXL} \sim M_{0E,2-comp} < M_{0E,SXL}$. The intra-to-extracellular exchange rate constant was $k_{IE} = 14 \text{ s}^{-1}$, with a lower bound of 5 s^{-1} . The upper bound was poorly defined since a fit with $k_{IE} = 14 \text{ s}^{-1}$ was not significantly different from that with k_{IE} approaching infinity. Thus a wide range of exchange rate constants fitted the data well and

it was difficult to determine a precise value, but based on the lower bound of 5 s^{-1} this voxel exhibited fast exchange.

Figure 6 shows the χ^2 value for the two-compartment fit with k_{IE} fixed to the value on the x-axis relative to the minimum χ_0^2 value. Figure 6a uses the data from Figure

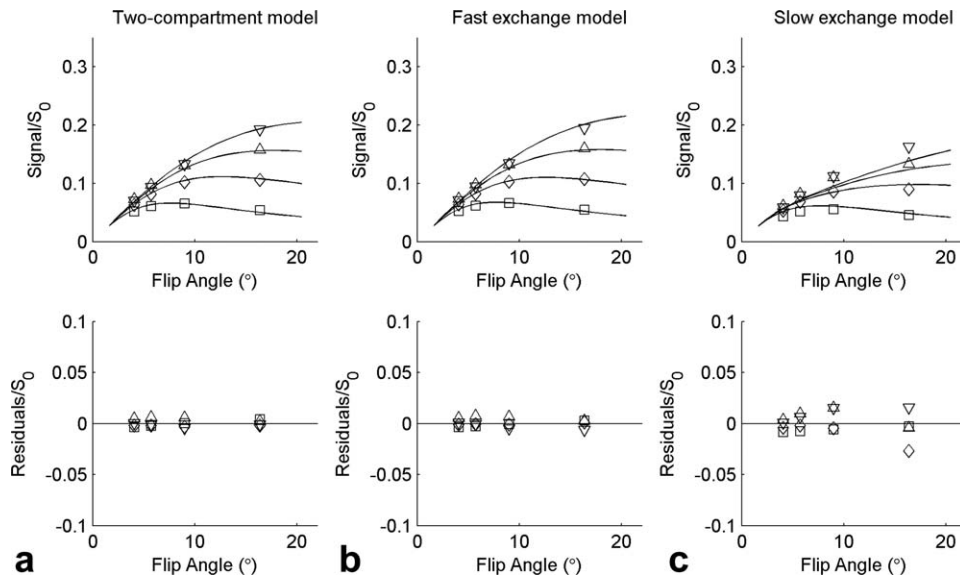


FIG. 5. Steady-state data for an included voxel with poorly defined upper error bound. There are four flip angles and four gadodiamide concentrations (cumulative amounts gadodiamide injected: squares—0 mmol; diamonds—0.05 mmol; triangles—0.15 mmol; inverted triangles—0.3 mmol) with fits (a) to the two-compartment model with water exchange (Eqs. [3]–[7]), (b) assuming infinitely fast exchange of water across the cell membrane (Eq. [15]) and (c) assuming no exchange of water across the cell membrane (Eq. [16]) shown by solid lines. Residuals are shown underneath the fits to demonstrate both the similarity of the two-compartment and FXL fits (χ_0^2 not significantly different) as well as the increased error and systematic bias of the SXL model (χ_0^2 1200% higher for SXL than two-compartment model). The intra-to-extracellular water exchange rate constant for the two-compartment fit is $k_{IE} = 14 (-9/+∞) \text{ s}^{-1}$.

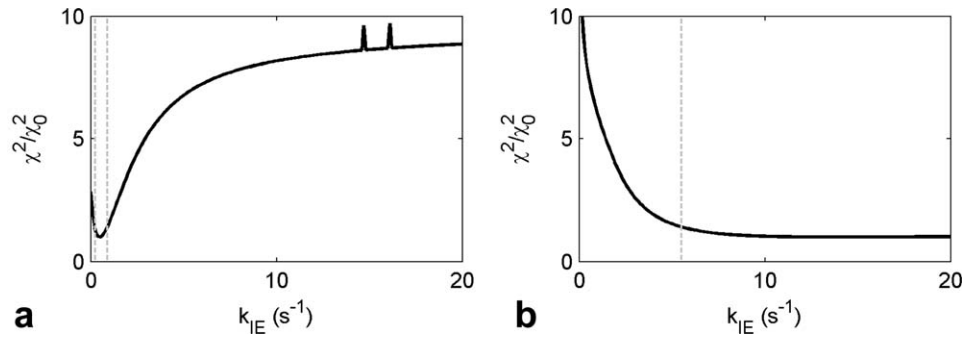


FIG. 6. The χ^2 values when intra-to-extracellular water exchange rate constant, k_{IE} , was set to a fixed value, as indicated on the x-axis. **a:** Data from Figure 4 with well-defined error bounds on the exchange rate parameter (gray dotted lines). Some jumps occur at higher exchange rate constants where the data fit poorly and the parameter space has local minima with similarly poor fits. **b:** Data from Figure 5 where the upper bound of the exchange rate constant was poorly determined, but a lower error bound can be set.

4 and the minimum is at $k_{IE} = 0.5 \text{ s}^{-1}$ with well-defined error bounds for the likely range of k_{IE} values (0.3–0.9 s^{-1} with 67% confidence). There is some jitter in the χ^2 values at higher k_{IE} since the fits are poor and local minima of similar goodness of fit exist. Figure 6b, for the data from Figure 5, demonstrates the case where the slow exchange fit was poor and a lower bound was placed on the intra-to-extracellular exchange rate constant (5 s^{-1} with 67% confidence), but the upper bound was poorly defined, with the χ^2 value remaining near its minimum even for the case of infinitely fast water exchange across the cell membrane. Over all animals, an average of $54 \pm 31\%$ of fitted voxels had substantially different fast exchange and two-compartment χ_0^2 values. The slow exchange model generally did not fit voxels well, with $70 \pm 27\%$ of SXL χ_0^2 values being substantially greater than the two-compartment χ_0^2 values.

Voxel-by-voxel maps of the two-compartment fit parameters for one animal are shown in the Supporting Information. The intracellular longitudinal relaxation rates, R_{1I} , ranged from ~ 0.3 to 0.7 s^{-1} . The extracellular water fraction, M_{0E} , and intra-to-extracellular water exchange rate constant, k_{IE} , showed heterogeneity within the tumor and are presented alongside histology in Figure 7.

General trends are apparent. Four animals have low extracellular water fractions and, as a result, relatively few voxels are mapped. Even in cases such as in the third animal, where extracellular water fraction is low throughout the tumor, there are differences in the exchange rate constant. Most voxels in viable tumor exhibited lower exchange rate constants and well-defined error bounds. Voxels in apoptotic regions tended to have higher intra-to-extracellular water exchange rates with high upper error bounds, although the lower bounds were larger than 3 s^{-1} , suggesting fast water exchange in these regions. This is emphasized by Table 1, which summarizes the extracellular water fractions and water exchange rates from all animals for regions of interest (ROIs) identified on histology as muscle (gastrocnemius), viable tumor (TUNEL-negative) and apoptotic (large TUNEL-positive regions). The voxels included in the parametric maps in these regions were used to calculate the range (minimum and maximum), mean, standard

deviation, median and interquartile range of the parameters in each animal and the numbers from all six animals were averaged to produce the values in the table. The exchange values in apoptotic regions, indicated by superscripts, appear artificially high, since they are fit equally well by the two-compartment and fast exchange models and have poorly determined upper error bounds.

The zoomed in view of the first tumor, shown in Figure 8, contains a smaller TUNEL-positive region with mixed apoptotic and normal cells (see arrow and histology insets). Significant cell clearance was not yet apparent. This region corresponded to an intermediate value of water exchange rate in the parametric map. The large necrotic region at the center of the tumor on the left side of the image has lower apparent extracellular water fraction due to lower amount of contrast agent reaching it, but still has high water exchange rate.

The results of fitting the first injection monitoring data to the DCE-MRI model, Eqs. [18] and [19], are shown in Figure 9. Figure 9a repeats the map of the extracellular water fraction, M_{0E} , from the steady-state fit. Figure 9b maps the extravascular extracellular volume fraction, v_e , from the Kety–Tofts model, which assumes fast exchange and is lower than M_{0E} in the viable tumor rim. Along the edge of the necrotic region at the tumor's center, v_e tends to extreme values since contrast agent uptake is low and the fit is insensitive to the value of v_e . Figure 9c shows the correlation between the steady-state parameter M_{0E} and the DCE parameter v_e for points outside these extremes ($0.01 < v_e < 1$). The color of the points indicates the intra-to-extracellular water exchange rate constant, with higher values ($k_{IE} > 3 \text{ s}^{-1}$) denoted by bright red and tending to cluster near the identity line. Slower water exchange rate constants, denoted by darker red points decreasing to black for values of 0 s^{-1} , tend to fall below the identity line.

DISCUSSION

Parametric maps were generated based on a two-compartment model of relaxation with water exchange in vivo. Contrast agent uptake was highly variable between animals and, as shown in Figure 2, heterogeneous within a given animal. Several tumor regions failed to reach

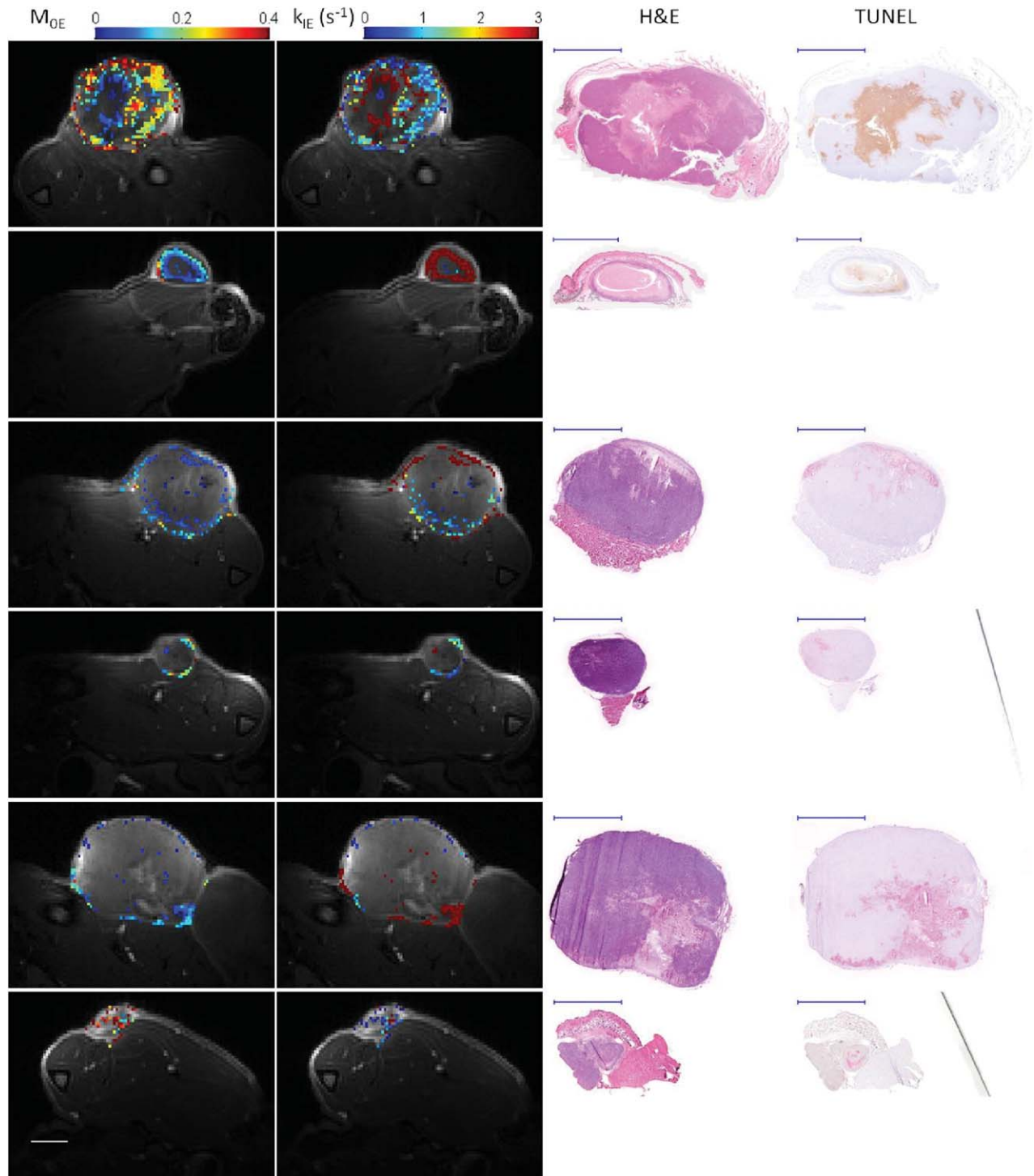


FIG. 7. Parametric maps of extracellular water fraction, M_{OE} , and intra-to-extracellular water exchange rate, k_{IE} , for all rats. Histology slices stained by H&E appear a darker, more intense purple in regions of higher cellularity. TUNEL staining indicates regions with DNA strand breaks (apoptosis), with positive staining appearing brown in the first two animals and pink in the later animals due to different fixation and staining methods. Scale bars represent 5 mm.

steady-state, but these were mainly located at the edges of large necrotic areas with little vasculature, where contrast agent leaked in slowly. Regions with low contrast agent uptake tended to be at the center of large necrotic areas or very cellular regions. Points with significant uptake were typically located near the tumor rim; this

has been noted in previous studies and attributed to lower perfusion in the tumor core, which is often necrotic (6,22,26,27). This suggests that although the exclusion criteria limited the regions in which the exchange rate constant was reliably determined, they also often had a physiological basis and these regions

Table 1

Summary of Extracellular Water Fractions, M_{0E} , and Water Exchange Rate Constants from Intracellular to Extracellular Space, k_{IE} , for Regions-of-Interest in Muscle (Gastrocnemius), Viable Non-apoptotic Tumor and Apoptotic Tumor

	Min	Max	Mean	SD	Median	IQR
M_{0E}						
Muscle	0.09	0.21	0.15	0.04	0.15	0.05
Viable tumor	0.13	0.20	0.17	0.02	0.17	0.03
Apoptotic tumor	0.07	0.16	0.10	0.03	0.09	0.05
k_{IE} (s^{-1})						
Muscle	0.2	1.0	0.6	0.3	0.5	0.4
Viable tumor	0.3	1.2	0.6	0.3	0.6	0.5
Apoptotic tumor	50.8 ^a	100.0 ^a	80.1 ^a	22.4 ^a	78.5 ^a	31.9 ^a

Only voxels included in the parametric maps were included in the calculation of statistics—minimum, maximum, mean, standard deviation (SD), median and interquartile range (IQR)—and the values from all six animals were averaged.

^aFor higher exchange rate constants, the upper error bound is poorly determined and the two-compartment χ_0^2 is not significantly different from that for fit with infinitely fast exchange. The exchange rate constants in these cases tend toward higher but more imprecise values.

might be characterized by other MRI methods. For example, regions of necrosis and where dead cells have already been cleared away are identifiable by increased water diffusion and increased T_2 , likely due to increased water content (28–30). The regions of most interest for early indications of cell death are better perfused, with better probability that the two-compartment model can be applied.

Some mapped regions demonstrated low extracellular water fraction, $< 5\%$, which was consistent with the high cellularity of many of the tumors. In regions where TUNEL staining was negative, indicating viable tumor, the average value of k_{IE} was $0.6 s^{-1}$. In TUNEL-positive regions, the water exchange rate constant was difficult to determine precisely, but was typically faster than $3 s^{-1}$ and voxels were fitted equally well by the two-compartment and fast exchange models. Even in cases

where there was not yet significant cell clearance, such as the region indicated by the arrow in Figure 8, the water exchange rate was elevated compared to surrounding viable tumor. This was consistent with in vitro results (4), which show an increase in the water exchange rate constant prior to cell clearance, due partly to increased surface area but mainly to an increase in membrane permeability during apoptosis.

There is no gold standard with which to compare the rate constants for exchange from the intra- to extracellular space in tumor from this study and there was large variation with tumor biology. From Table 1, the intra-to-extracellular water exchange rate constant in viable tumor regions, $0.6 \pm 0.3 s^{-1}$, is within the range found in other preclinical models: $0.79 \pm 0.16 s^{-1}$ in rat brain glioma (22), $1.2\text{--}2 s^{-1}$ in mammary carcinoma xenografts in mice (23), $4.2 \pm 8.8 s^{-1}$ in RIF-1 xenografts in mice (24) and $0.7 s^{-1}$ in rat brain glioma although the variation in this last case is large (6).

A more reliable comparison might be done with the parameters in muscle. For gastrocnemius, the extracellular water fraction $M_{0E} = 0.15 \pm 0.04$ and intra-extracellular water exchange rate constant $k_{IE} = 0.6 \pm 0.3 s^{-1}$ agree with the muscle values of $M_{0E} = 0.11$ and $k_{IE} = 1.1 \pm 0.4 s^{-1}$ in Sprague–Dawley rats (5). In addition, the low variability in muscle values across animals and the reproducibility in a given animal over a number of days suggest the method is robust.

The fit errors calculated using Eq. [14] for the equilibrium signal, S_0 , the intracellular T_1 relaxation rate, R_{1I} , and the extracellular water fraction, M_{0E} , were less than the standard deviation across the tumor, indicating that the biological variation was greater than that from the fitting procedure. For the intracellular-to-extracellular water exchange rate constant, k_{IE} , this was not always the case, but the low precision of this parameter was not due to poor SNR. Rather, the statistical error in the fitting of the exchange rate constant depends on how fast the water exchange rate is relative to the relaxation taking place during the experiment, with the FXL applying in cases meeting the criteria described by Eq. [9]. In cases where the contrast agent concentration was low,

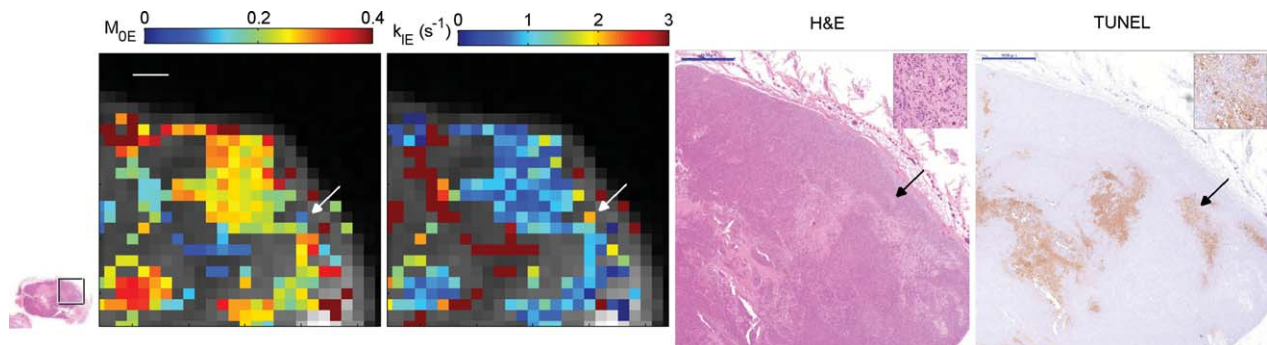


FIG. 8. Close up of the upper right portion of the tumor of the first rat from Figure 7, as indicated by the white box in the small histology image on the left. The upper right part of the map has higher extracellular water fraction than the lower right part of the tumor and is associated with lower cellularity on the H&E staining. Regions at the middle and left of this part of the tumor, where TUNEL staining indicates apoptosis, have higher water exchange rate constants, whereas regions along the tumor rim appear normal and have lower water exchange rate constants. The region indicated by the arrow, shown in the insets on histology, contains a mix of normal and apoptotic cells with intermediate exchange rate. Scale bars represent 1 mm.

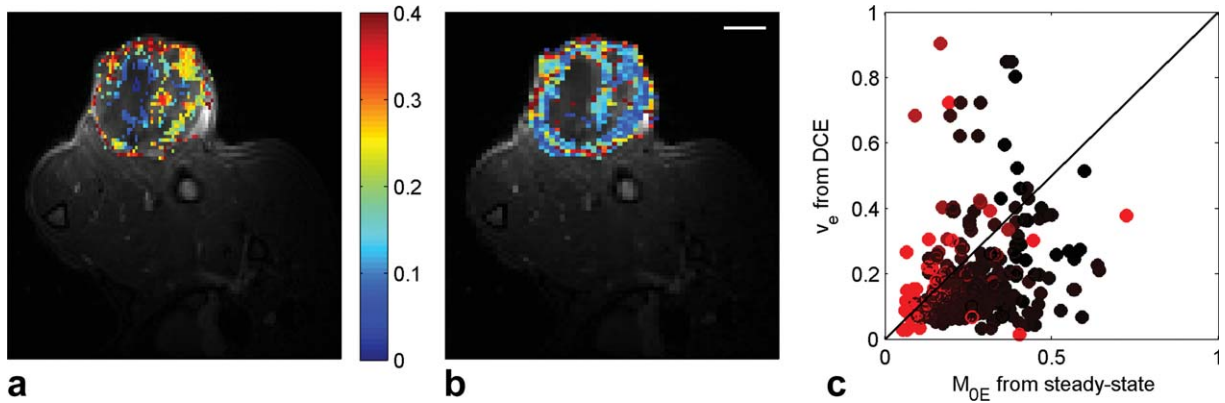


FIG. 9. Comparison of (a) the extracellular water fraction, M_{0E} , from the fit of the steady-state data to the two-compartment model of relaxation with exchange and (b) the extravascular extracellular volume fraction, v_e , from the fit of the DCE-MRI data to the Kety–Tofts model. The Kety–Tofts model assumes fast exchange and the v_e parameter is typically less than or equal to the steady-state M_{0E} parameter except in large necrotic areas near the tumor center where DCE-MRI data are described by a single compartment. c: Correlation plot of v_e and M_{0E} . Data with fast exchange rate constants from the two-compartment fit (bright red) cluster along the black identity line. Voxels with slower exchange rate constants (darker red and black) cluster below the line. Scale bar represents 5 mm and both maps have the same color scale.

the difference between the intra- and extracellular longitudinal relaxation rates was not as large and the value of exchange was poorly determined. It may be possible, as in Figure 6b, to place some lower bound on the exchange rate constant, but the upper bound will be large. The error bounds tended to be narrower for slower exchange rates, which were better-determined at low contrast agent concentrations. Similar precision issues have been noted in other attempts to map water exchange *in vivo*. For example, Yankeelov et al. (6) found that contrast agent uptake in normal-appearing rat brain was too low to allow the water exchange rate constant to be precisely determined and water exchange appeared infinitely fast, in spite of much better-determined values in the surrounding muscle. This work emphasizes the importance of calculating the statistical errors in the fit, particularly for the exchange rate constant, in order to determine a reliable range. In cases where the range was large and included low values, the exchange rate constants were not mapped since they were not reliable. *In vitro* experiments showed intracellular T_2 relaxation rates that were much faster than extracellular rates (4). If this is the case *in vivo*, experiments measuring T_2 relaxation will be more sensitive to exchange at low contrast agent concentrations and move toward the FXL at higher concentrations. Acquiring T_2 data in addition to T_1 data would then prove useful for determining water exchange more precisely, albeit at the expense of increased scan time.

Mapped voxels fell into two cases: those similar to Figure 4, where incorporating water exchange resulted in a statistically improved fit; and those like Figure 5, where the fast exchange assumption was valid and sufficient. Correctly applying the fast exchange assumption was important for accurate determination of the other parameters. In Figure 5, the extracellular water fraction values from the fast exchange and two-compartment fits were similar. However, the fits in Figure 4 resulted in an increase in the estimated extracellular water fraction when slower exchange rates were assumed, $M_{0E,FXL} < M_{0E,2-comp} < M_{0E,SXL}$, as has been observed in previous

studies (7,27). It was therefore necessary to use a more complex model that incorporated exchange in these cases. This model not only corrected the underestimation of the extracellular water fraction, which was important since these voxels were more likely to be present in viable tumor, but also yielded a value for the exchange itself, which is a marker of apoptosis.

Previous studies have evaluated the water exchange rate constant using modified DCE-MRI methods (5,6,22–25). The temporal resolution requirements for DCE-MRI, particularly near the peak when contrast agent concentration is highest, require the use of shorter repetition times, TR. Such methods often have low precision (7) or show no sensitivity (25) to exchange, even when multiple flip angles are used. The steady-state method employed in this article is affected by contrast agent washout, but this temporal restriction is not as stringent as in a DCE-MRI modelling experiment. The steady-state method takes ~ 15 min, most of which is waiting for steady-state following each bolus injection; this is longer than a single-injection DCE-MRI measurement, but faster than preclinical methods that employ a constant infusion (5) that can take ~ 2 h to reach steady-state for multiple concentrations, although the current method uses a sevenfold higher contrast agent dose delivery rate than the constant infusion work. Furthermore, the steady-state method does not rely on the rapidly changing initial part of the uptake curve nor does it rely on an arterial input function, which is a particular challenge for DCE-MRI experiments in small animals. Instead, an assumption about the steady-state contrast agent concentration was made based on (1) a pre-established time constant for clearance by the kidneys during the experiment and (2) distribution of contrast agent throughout a constant volume following each injection.

The clearance half-life was assumed to be ~ 20 minutes, which was supported both by prior pharmacokinetic experiments in this rat species and by existing literature values (13–15,31). There may be some variation in contrast agent clearance between individual rats,

producing a systematic error in the concentration of gadodiamide in the extracellular space calculated by Eq. [12]. This affects the extracellular longitudinal relaxation rate, R_{1E} , used in the model and may result in systematic error in the fit parameters. However, the experimental design minimized the effects of clearance by increasing the amount of gadodiamide with each injection (0.05 mmol for the first injection, 0.10 mmol for the second injection and 0.15 mmol for the third injection) so that the largest contribution of gadodiamide was from the most recent injection. Simulations (not shown) indicate that assuming no clearance produces <1% change in R_{1I} , 10% change in M_{0E} and 5% change in k_{IE} . Thus even large errors in the estimated clearance half-life of the contrast agent produce only modest changes in the final fitted parameters.

The distribution volume estimate, $V_{\text{dist}} \approx 20\%$ rat volume using the mass and a density of 1 g/mL, in Eq. [12] was also based on pharmacokinetic studies, which showed a distribution volume of 19–31% and this was consistent with literature values of 17–31% (13,15,31). Simulations (not shown) indicated that the extracellular gadodiamide concentration, estimated based on the distribution volume, was mainly coupled to the extracellular water fraction, M_{0E} . The agreement of muscle values with the literature, however, suggests the 20% assumption was reasonable in these animals. Additional scans may be added to the exam to quantify contrast agent concentration in blood and these would not have the same temporal resolution constraints as those used more commonly in DCE-MRI experiments. Some animals did demonstrate a gradient of M_{0E} values at the edges of necrotic areas (e.g., the center of the first tumor in Fig. 7) where contrast agent diffused into the center more slowly. This results in a lower steady-state contrast agent concentration than surrounding areas, even though the regions meet the exclusion criterion of steady-state slope on the DCE images, and the modelled M_{0E} parameter appears artificially low due to coupling between M_{0E} and $[Gd]_E$ in Eqs. [7] and [8]. More stringent steady-state exclusion criteria might correct this, but otherwise extracellular water fractions show good correspondence with histology, suggesting that biological heterogeneity and changes following treatment within a particular animal may still be informative.

It was assumed that gadodiamide did not leak across the cell membrane in cells undergoing apoptosis. This assumption was examined by mass spectroscopy in acute myeloid leukemia cells in vitro and intracellular concentrations were found to be less than 0.7% of extracellular concentrations at late stages of apoptosis (4), which included membrane shape alterations and blebbing, although the possibility of significant leakage of gadodiamide into cells at very late apoptotic stages cannot be excluded.

The relaxivity in the extracellular space was assumed to be the same as that in blood plasma. This is the case in some tissues (32), but there is some variation in relaxivity with macromolecular content (33,34) that could bias the absolute parameter values. However, if the treatment does not substantially alter the macromolecular

content of the extracellular space during the monitoring period, relative parameter values may still be compared.

The parameters obtained from the steady-state method were compared to those obtained by a more conventional DCE-MRI method and fit to the Kety–Tofts model. This demonstrated that the multiinjection method provided additional information. In the FXL, the extracellular water fraction from the two-compartment model and steady-state data, M_{0E} , and extravascular extracellular water fraction, v_e , typically agreed, falling near the identity line in Figure 9c. This is expected since the Kety–Tofts model assumes fast water exchange. When exchange was slower, M_{0E} was typically higher than v_e , except in cases near the edges of large necrotic areas where the DCE-MRI fit is hindered by poor uptake. The extravascular extracellular volume fraction, v_e , and water fraction, M_{0E} , are not precisely the same parameter: M_{0E} relates to the water concentration in the extracellular space while v_e is related to the physical space into which the contrast agent leaks, independent of water concentration. Nevertheless, the steady-state method had some discrepancies with the DCE-MRI fits, which appear to be explained by the differing exchange rates, as has been noted previously by Landis et al. (27) and Buckley et al. (7).

It should also be noted that many of the literature studies examining exchange use it for the purpose of quantifying the error that incorrect exchange assumptions produce in the other pharmacokinetic model parameters, such as the volume transfer constant, K_{trans} , and the extravascular extracellular volume fraction, v_e . Several groups have suggested methods for minimizing exchange when the kinetics of the contrast agent are of primary interest (35), but this work demonstrates that for the purposes of detecting apoptosis and monitoring response to treatment, the exchange rate constant itself was a valuable biomarker.

In this study, we assumed that the contribution of the blood volume to the signal change was negligible. This is a common assumption in many DCE-MRI studies and valid when the volume fraction of the plasma is small relative to the volume fraction of the extravascular extracellular space (36). This is not the case in all tumor types, however. Simulations of the effect of blood volume on steady-state data (not shown) were performed using parameter values of $R_{1I} = 0.56 \text{ s}^{-1}$, $M_{0E} = 0.2$ and $k_{IE} = 1$ and 5 s^{-1} . Fast water exchange between red blood cells and plasma, a haematocrit of 0.4 and slow water exchange across the blood vessel wall were assumed. The simulations indicated that a blood volume of 10% changed equilibrium signal, S_0 , less than 1% and the intracellular longitudinal relaxation rate, R_{1I} , less than 5%. The strongest coupling with the blood volume was with the extracellular water fraction, as might be expected for data acquired in the steady-state region of contrast agent uptake, where the plasma and extravascular extracellular concentrations of contrast agent are equal. Neglecting a blood volume of 10% in the fitting resulted in an overestimation of the extracellular water fraction, M_{0E} , of 18% when water exchange was fast ($k_{IE} = 5 \text{ s}^{-1}$). The exchange rate constant for water moving from the intracellular to extracellular space, k_{IE} , was

overestimated by 10% in this case. Both of these errors increased at lower water exchange rates ($k_{IE} = 1 \text{ s}^{-1}$), to 26% overestimation for M_{OE} and 20% overestimation for k_{IE} . Thus it may be necessary to account for blood volume in more vascular tumor types.

The average cumulative dose of gadodiamide injected into the rats in this study was 1.7 mmol/kg, much higher than a clinical dose of 0.1 mmol/kg. Even with this dose, exchange could not be well-determined in some regions where the extracellular space available for gadodiamide to fill was small. For example, some tumors showed extracellular water fractions less than 0.05. However, the muscle data, with a water fraction of 0.15 ± 0.04 , tended to have more reliably fitted exchange rate constants. Translational work should therefore focus on more vascular and less cellular tumor types, such as renal cell carcinoma. Although the error bounds of the exchange rate constant may be larger due to lower gadodiamide concentrations and hinder exact quantification, it may still be possible to approximate exchange and observe regions where exchange becomes fast following treatment. Renal tumors are also in close proximity to the descending aorta, which has potential for quantification of the contrast agent concentration from the MR images, rather than using a weight-based assumption. Quantifying the extracellular contrast agent concentration should therefore be more feasible in a clinical setting than it is with small animals.

A small number of animals with a single tumor type were presented as a proof of principle. These findings are therefore preliminary and should be replicated in more animals and other tumor types to confirm the interpretation of the data.

As treatment induces apoptosis in cells, the water exchange rate is expected to increase (4). As described above, higher water exchange rates are more difficult to determine precisely, so that the number of voxels with reliably determined exchange may decrease following treatment. This was somewhat mitigated by the exclusion criteria, which allowed for poorly determined upper bounds (approaching infinity), as long as the lower bound was high enough ($> 3 \text{ s}^{-1}$). Nevertheless, the statistical errors in the fit emphasize that caution is needed when interpreting results from a region of interest over time, as occurs during treatment monitoring. Parametric mapping with error analysis at each treatment stage is preferable, although this process is more time-intensive.

CONCLUSIONS

A two-compartment model of relaxation with water exchange between the intra- and extracellular spaces was applied to data obtained in the late-uptake stages following three separate contrast agent injections into rats with breast cancer tumor xenografts, when contrast agent concentration was relatively constant. Comparison of parametric maps of the two-compartment model parameters revealed that the extracellular water fraction had good correspondence with cellular density and regions with high intra-to-extracellular water exchange rate constant corresponded to regions that stained positive for apoptosis. The water exchange rate maps contained information

that was not always evident from the water fractions, with elevated values in regions where mixed nonapoptotic and apoptotic cells were present, even before significant cell clearance was visible on H&E staining. Extracellular water fraction and water exchange rate values for muscle were in agreement with those from the literature.

Examining the statistical errors in the fitting procedure was an important step in the analysis. Regions with lower tissue contrast agent concentration, typically due to low vascularity or high cellularity (small contrast-containing extracellular space), have similar goodness of fit for a wide range of exchange rate constants, making that parameter poorly determined in such cases. However, these regions often correspond to necrotic areas detectable by other methods. In viable regions, typically along the tumor rim, the water exchange rate constants have promise as a marker of apoptosis and thus of indicating response to treatment.

ACKNOWLEDGMENTS

The authors would like to thank Krista Holdsworth and others who assisted with animal handling. This study was funded by the National Cancer Institute of Canada and Canadian Institutes of Health Research, Terry Fox Programme.

REFERENCES

- Blankenberg FG, Tait JF, Strauss HW. Apoptotic cell death: its implications for imaging in the next millennium. *Eur J Nucl Med* 2000;27:359–367.
- Ellis PA, Smith IE, McCarthy K, Detre S, Salter J, Dowsett M. Preoperative chemotherapy induces apoptosis in early breast cancer. *Lancet* 1997;349:849.
- Symmans WF, Volm MD, Shapiro RL, et al. Paclitaxel-induced apoptosis and mitotic arrest assessed by serial fine-needle aspiration: implications for early prediction of breast cancer response to neoadjuvant treatment. *Clin Cancer Res* 2000;6:4610–4617.
- Bailey C, Giles A, Czarnota GJ, Stanisz GJ. Detection of apoptotic cell death *in vitro* in the presence of Gd-DTPA-BMA. *Magn Reson Med* 2009;62:46–55.
- Landis CS, Li X, Telang FW, Molina PE, Palyka I, Vetek G, Springer CS. Equilibrium transcytolemmal water-exchange kinetics in skeletal muscle *in vivo*. *Magn Reson Med* 1999;42:467–478.
- Yankeelov TE, Rooney WD, Li X, Springer CS. Variation of the relaxographic “shutter-speed” for transcytolemmal water exchange affects the CR bolus-tracking curve shape. *Magn Reson Med* 2003;50:1151–1169.
- Buckley DL, Kershaw LE, Stanisz GJ. Cellular-interstitial water exchange and its effect on the determination of contrast agent concentration *in vivo*: dynamic contrast-enhanced MRI of human internal obturator muscle. *Magn Reson Med* 2008;60:1011–1019.
- Christensen KA, Grant DM, Schulman EM, Walling C. Optimal determination of relaxation times of Fourier transform nuclear magnetic resonance. Determination of spin-lattice relaxation times in chemically polarized species. *J Phys Chem* 1974;78:1971–1977.
- McConnell HM. Reaction rates by nuclear magnetic resonance. *J Chem Phys* 1958;28:430–431.
- Woessner D. Nuclear transfer effects in nuclear magnetic resonance pulse experiments. *J Chem Phys* 1961;35:41–48.
- Benga G. Water transport in red blood cell membranes. *Prog Biophys Mol Biol* 1988;51:193–245.
- Kety SS. The theory and applications of the exchange of inert gas at the lungs and tissues. *Pharmacol Rev* 1951;3:1–41.
- McIntyre DJO, Ludwig C, Pasan A, Griffiths JR. A method for interleaved acquisition of a vascular input function for dynamic contrast-enhanced MRI in experimental rat tumours. *NMR Biomed* 2004;17:132–43.

14. Maxwell RJ, Wilson J, Prise VE, Vojnovic B, Rustin GJ, Lodge MA, Tozer GM. Evaluation of the anti-vascular effects of combretastatin in rodent tumours by dynamic contrast enhanced MRI. *NMR Biomed* 2002;15: 89–98.
15. Weidensteiner C, Rausch M, McSheehy PMJ, Allegrini PR. Quantitative dynamic contrast-enhanced MRI in tumor-bearing rats and mice with inversion recovery TrueFISP and two contrast agents at 4.7 T. *J Magn Reson Imaging* 2006;24:646–656.
16. Chang L-C, Koay CG, Basser PJ, Pierpaoli C. Linear least-squares method for unbiased estimation of T1 from SPGR signals. *Magn Reson Med* 2008;60:496–501.
17. Chavez S, Stanisz GJ. A novel method for simultaneous 3D B1 and T1 mapping: the method of slopes (MoS). *NMR Biomed* 2012;25: 1043–1055.
18. Lausch A, Ebrahimi M, Martel AL. Image registration for abdominal dynamic contrast-enhanced magnetic resonance images. In *Proceeding of the 8th IEEE Symposium on Biomedical Imaging: From Nano to Macro*, Chicago, IL, USA, 2011. p. 561–565.
19. Gupta RK, Ferretti JA, Becker ED, Weiss GH. A modified fast inversion-recovery technique for spin-lattice relaxation measurements. *J Magn Reson* 1980;38:447–452.
20. Bevington PR, Robinson DK. *Data reduction and error analysis for the physical sciences*. Third Ed. Boston: McGraw-Hill; 2003.
21. Tofts PS, Kermode AG. Measurement of the blood-brain barrier permeability and leakage space using dynamic MR imaging. 1. Fundamental concepts. *Magn Reson Med* 1991;17:357–367.
22. Pickup S, Chawla S, Poptani H. Quantitative estimation of dynamic contrast enhanced MRI parameters in rat brain gliomas using a dual surface coil system. *Acad Radiol* 2009;16:341–350.
23. Yankeelov TE, Luci JJ, DeBusk LM, Lin PC, Gore JC. Incorporating the effects of transcytolemmal water exchange in a reference region model for DCE-MRI analysis: theory, simulations, and experimental results. *Magn Reson Med* 2008;59:326–335.
24. Zhou R, Pickup S, Yankeelov TE, Springer CS, Glickson JD. Simultaneous measurement of arterial input function and tumor pharmacokinetics in mice by dynamic contrast enhanced imaging: effects of transcytolemmal water exchange. *Magn Reson Med* 2004;52:248–257.
25. Bains LJ, McGrath DM, Naish JH, et al. Tracer kinetic analysis of dynamic contrast-enhanced MRI and CT bladder cancer data: a preliminary comparison to assess the magnitude of water exchange effects. *Magn Reson Med* 2010;64:595–603.
26. Donahue KM, Weisskoff RM, Parmelee DJ, Callahan RJ, Wilkinson RA, Mandeville JB, Rosen BR. Dynamic Gd-DTPA enhanced MRI measurement of tissue cell volume fraction. *Magn Reson Med* 1995; 34:423–432.
27. Landis CS, Li X, Telang FW, et al. Determination of the MRI contrast agent concentration time course in vivo following bolus injection: effect of equilibrium transcytolemmal water exchange. *Magn Reson Med* 2000;44:563–574.
28. Lemaire L, Franconi F, Saint-Andre JP, Roullin VG, Jallet P, Le Jeune JJ. High-field quantitative transverse relaxation time, magnetization transfer and apparent water diffusion in experimental rat brain tumour. *NMR Biomed* 2000;13:116–123.
29. Chenevert TL, McKeever PE, Ross BD. Monitoring early response of experimental brain tumors to therapy using diffusion magnetic resonance imaging. *Clin Cancer Res* 1997;3:1457–1466.
30. Valonen PK, Lehtimäki KK, Väisänen TH, Kettunen MI, Gröhn OHJ, Ylä-Herttuala S, Kauppinen RA. Water diffusion in a rat glioma during ganciclovir-thymidine kinase gene therapy-induced programmed cell death in vivo: correlation with cell density. *J Magn Reson Imaging* 2004;19:389–396.
31. Wedeking P, Eaton S, Covell DG, Nair S, Tweedle MF, Eckelman WC. Pharmacokinetic analysis of blood distribution of intravenously administered 153Gd-labeled Gd(DTPA)2- and 99mTc(DTPA) in rats. *Magn Reson Imaging* 1990;8: 567–575.
32. Donahue KM, Burstein D, Manning WJ, Gray ML. Studies of Gd-DTPA relaxivity and proton exchange rates in tissue. *Magn Reson Med* 1994;32:66–76.
33. Shuter B, Tofts P, Wang S, Pope J. The relaxivity of Gd-EOB-DTPA and Gd-DTPA in liver and kidney of the Wistar rat. *Magn Reson Imaging* 1996;14:243–253.
34. Stanisz GJ, Henkelman RM. Gd-DTPA relaxivity depends on macromolecular content. *Magn Reson Med* 2000;44:665–667.
35. Donahue KM, Weisskoff RM, Chesler DA, Kwong KK, Bogdanov AA, Mandeville JB, Rosen BR. Improving MR quantification of regional blood volume with intravascular T1 contrast agents: accuracy, precision, and water exchange. *Magn Reson Med* 1996;36: 858–867.
36. Tofts PS, Brix G, Buckley DL, et al. Estimating kinetic parameters from Dynamic Contrast-Enhanced T1-weighted MRI of a diffusable tracer: Standardized quantities and symbols. *J Magn Reson Imaging* 1999;10: 223–232.